

1 **Revision 1**

2 Word count: 7535

3 **Structure and compressibility of Fe-bearing Al-phase D**

4 Giacomo Criniti^{1,*}, Takayuki Ishii², Alexander Kurnosov¹, Konstantin Glazyrin³, Rachel J. Husband³,
5 Tiziana Boffa Ballaran¹

6 ¹Bayerisches Geoinstitut, University of Bayreuth, 95440 Bayreuth, Germany

7 ²Center for High Pressure Science and Technology Advanced Research, Beijing, 100094, China

8 ³Deutsches Elektronen-Synchrotron DESY, Notkestr. 85, 22607 Hamburg, Germany

9 * Corresponding author: giacomo.criniti@uni-bayreuth.de

Abstract

Due to its large thermal stability, Al-phase D, the $(\text{Al}, \text{Fe}^{3+})_2\text{SiO}_6\text{H}_2$ member of the dense hydrous magnesium silicate (DHMS) phase D, may survive along hot subduction geotherms or even at ambient mantle temperatures in the Earth's transition zone and lower mantle, playing therefore a major role as water reservoir and carrier in the Earth's interior. We have investigated the crystal structure and high-pressure behavior of Fe-bearing Al-phase D with a composition of $\text{Al}_{1.53(2)}\text{Fe}_{0.22(1)}\text{Si}_{0.86(1)}\text{O}_6\text{H}_{3.33(9)}$ by means of single-crystal X-ray diffraction. While the structure of Al-phase D ($\text{Al}_2\text{SiO}_6\text{H}_2$) has space group $P6_3/mcm$ and consists of equally populated and half-occupied $(\text{Al}, \text{Si})\text{O}_6$ octahedra, Fe-incorporation in Al-phase D seems to induce partial ordering of the cations over the octahedral sites, resulting in a change of the space group symmetry from $P6_3/mcm$ to $P6_322$ and in well-resolved diffuse scattering streaks observed in X-ray images. The evolution of the unit cell volume of Fe-bearing Al-phase D between room pressure and 38 GPa, determined by means of synchrotron X-ray diffraction in a diamond anvil cell, is well described by a 3rd-order Birch-Murnaghan equation of state having isothermal bulk modulus $K_{\text{T}0} = 166.3(1.5)$ GPa and first pressure derivative $K'_{\text{T}0} = 4.46(12)$. Above 38 GPa, a change in the compression behavior is observed, likely related to the high-to-low spin crossover of octahedrally coordinated Fe^{3+} . The evolution of the unit cell volume across the spin crossover was modelled using a recently proposed formalism based on crystal-field theory, which shows that the spin crossover region extends from about 30 to 65 GPa. Given the absence of abrupt changes in the compression mechanism of Fe-bearing Al-phase D before the spin crossover, we show that the strength of H-bonds and likely their symmetrization do not greatly affect the elastic properties of phase D solid solutions, independently of their compositions.

Keywords: DHMS, phase D, X-ray diffraction, equation of state, spin crossover

Introduction

The stability of dense hydrous magnesium silicates (DHMS) at high-pressure and high-temperature conditions has been extensively studied for more than 20 years as these phases yield the potential to carry and recycle water from Earth's surface to its deep interior (e.g. Frost 2006; Nishi et al. 2014; Ohtani et al. 2014). The crystal structure of DHMS generally consists of hexagonal closest-packed (*hcp*) layers of O atoms with Mg and Si occupying interstitial octahedral and tetrahedral sites, respectively. However, in phase D and phase H, which are stable under mantle transition zone and lower mantle conditions, Si displays octahedral coordination, allowing partial (Yang et al. 1997) or complete (Bindi et al. 2014) mixing with Mg to take place. Al incorporation in the crystal structures of these two phases further promotes cation mixing at octahedral sites and enhances their thermal stability, allowing Al-bearing phase D and phase H to potentially survive along hot subduction geotherms or even at ambient mantle temperatures in the transition zone and lower mantle (Ohira et al. 2014; Pamato et al. 2015).

In the end member Mg-phase D (space group $P\bar{3}1m$), with nominal composition $\text{MgSi}_2\text{O}_6\text{H}_2$, Mg and Si occupy distinct octahedral sites, named M1 and M2, respectively, located on alternated interstitial layers of the oxygen *hcp* sublattice (Yang et al. 1997). M2 octahedra are connected with one another through one edge and to M1 octahedra through vertices, while M1 octahedra are separated from one another and share vertices with M2 octahedra (Supplementary Figure S1a). The remaining two octahedral sites, i.e. M3 and M4, share faces with M2 and M1, respectively, and are nominally vacant in Mg-phase D. Previous studies showed that the crystal structure of phase D becomes progressively disordered in the proximity of its Al-end member (Boffa Ballaran et al. 2010; Pamato et al. 2015). As Al is incorporated in the structure of phase D via the $\text{Mg}^{2+} + \text{Si}^{4+} = 2\text{Al}^{3+}$ substitution, not only this cation substitutes in both M1 and M2, but also causes a partial redistribution of the cations in the M3 and M4 sites. In a Al-rich phase D sample having $\text{Mg} + \text{Fe} = 0.3$ atoms per formula unit, cation disordering was observed in the

form of partially occupied, but not equally populated M2 and M3 sites, while M1 showed full occupancy and M4 appeared vacant (Boffa Ballaran et al. 2010). In Mg- and Fe-free Al-phase D (Supplementary Figure S1b), nominally $\text{Al}_2\text{SiO}_6\text{H}_2$, the distribution of Al and Si over the cation sites is completely random (Pamato et al. 2015) and, as a consequence, the space group symmetry increases from $P\bar{3}1m$ to $P6_3/mcm$. From the structural refinement of Al-phase D, it was also found that the Pauling bond strength of O atoms is +1.42, which is significantly smaller than in Mg-phase D (i.e. +1.67) and suggests that stronger covalent bonds O–H and hydrogen bonds (or H-bonds) $\text{O}\cdots\text{H}$ are formed as a result of Al substitution and cation disordering.

In a recent publications, the pressure induced symmetrization of H-bonds was reported in CaCl_2 -structured δ - AlOOH (Sano-Furukawa et al. 2018). Phase δ is stable in hydrous basaltic systems at lower mantle pressures, where it forms solid solutions with MgSiO_4H_2 phase H (Ohira et al. 2014; Liu et al. 2019). Owing to its strong symmetric H-bonds, the bulk modulus of δ - AlOOH was found to substantially increase across the symmetrization (Sano-Furukawa et al. 2009; Satta et al. 2021), to the point that the presence of δ -H solid solutions in hydrous subducted basalt can produce a 1.5% increase in its seismic velocities with respect to dry basalt at topmost lower mantle pressures (Satta et al. 2021). While it is still controversial whether a pressure induced H-bond symmetrization takes place in Mg-phase D and whether it affects its elastic properties (Hushur et al. 2011; Rosa et al. 2013), H-bonds in Al-phase D are known to be stronger than in Mg-phase D already at ambient conditions (Pamato et al. 2015). However, previous experimental studies on the compressibility of phase D were conducted only on samples rich in Mg, hampering our understanding of how strongly the H-bonds affect the bulk modulus systematics of phase D solid solutions and whether the H-bond symmetrization influences the high-pressure structural evolution of phase D, similarly to what has been observed for phase δ -H. To assess this possibility, we investigated the crystal structure of single-crystal Fe-bearing Al-phase D at ambient conditions using X-ray diffraction,

with particular emphasis on the relation between cation disordering and strength of H-bonds. Additionally, the high-pressure behavior of Fe-bearing Al-phase D was determined for the first time using diamond anvil cells (DAC) and synchrotron X-ray diffraction, providing insights on the relation between H-bond symmetrization, spin state of Fe, and elasticity of phase D solid solutions at high pressure.

Experimental methods

Sample synthesis and characterization

Fe-bearing Al-Phase D was synthesized at 27 GPa and 1673 K in the 15-MN Kawai-type multi-anvil apparatus with the Osugi-type (DIA) guide block system, IRIS-15, installed at the Bayerisches Geoinstitut, University of Bayreuth (Ishii et al. 2016, 2019; Liu et al. 2017). The starting material, consisting of a finely ground mixture of SiO₂, Al(OH)₃ and Fe₂O₃ in molar proportion 2:6:1, was loaded in a Pt tube capsule that was then sealed by welding. A LaCrO₃ heater was inserted in a Cr₂O₃-doped MgO octahedron with 7 mm edge length, which served as pressure medium. WC cubes having 3 mm truncated edge length were employed for high pressure generation and compressed to a load of 13 MN. The sample was heated for 3 h, quenched by cutting the electric power supply and slowly decompressed to ambient conditions in 12 h. The recovered sample consisted of coexisting Fe-bearing Al-phase D (light brown color and up to about 150 μm in their longest directions) and δ-(Al,Si,Fe)OOH (brown-blue pleochroism under polarized light and up to 200 μm in size), identified by single-crystal X-ray diffraction.

Inclusion free samples of Fe-bearing Al-phase D were embedded in epoxy for textural and chemical analyses. Backscattered electron (BSE) images were acquired using a LEO Gemini 1530 scanning electron microscope (SEM) and showed that the samples are chemically homogeneous. The chemical compositions of several phase D crystals were determined using a JEOL JXA-8200 electron probe microanalyzer (EPMA) operated at an acceleration voltage of 15 kV and a beam current of 5 nA.

99 Enstatite was used as a standard for Si, corundum for Al and metal iron for Fe, while the H₂O concentration
100 was determined as the difference between 100% and the observed EPMA totals. The average composition
101 was calculated from a total of 51 measurements on 6 different crystals and resulted to be
102 $\text{Al}_{1.53(2)}\text{Fe}_{0.22(1)}\text{Si}_{0.86(1)}\text{O}_6\text{H}_{3.33(9)}$, where the numbers between parentheses indicate one standard deviation
103 on the last digit. To determine the valence of Fe in the sample, Mössbauer spectroscopy (MS)
104 measurements were performed on a mosaic of several hand-picked single crystals of Fe-bearing Al-phase
105 D using a constant acceleration spectrometer in combination with a point ^{57}Co source (McCammon 1994).
106 A Ta mask with a 500 μm hole was applied in front of the sample because of the limited amount of material
107 available. The Mössbauer spectrum of Fe-bearing Al-phase D (Figure 1) was collected over 7 days and
108 fitted with one asymmetric Lorentzian doublet using MossA (Prescher et al. 2012). The determined isomer
109 shift (IS) of 0.34(2) mm/s and quadrupole splitting (QS) of 0.63(2) mm/s are consistent with those of Fe^{3+}
110 found in previous studies for Fe-Al-bearing Mg-phase D samples (Chang et al. 2013; Wu et al. 2016).

111 **Single-crystal X-ray diffraction at ambient conditions**

112 Single crystals of Fe-bearing Al-phase D were observed under a polarizing microscope and
113 selected for X-ray diffraction measurements based on their sharp optical extinction and the absence of
114 visible twinning and inclusions. A crystal with dimensions 120 x 70 x 60 μm^3 was analyzed at ambient
115 conditions using a Huber single-crystal diffractometer equipped with a point detector and operated by the
116 SINGLE software (Angel & Finger, 2011) for precise and accurate lattice parameters determination. The
117 diffractometer employed a $\text{MoK}\alpha$ tube operated at 50 kV and 40 mA. Typical diffraction profiles measured
118 upon ω -scan rotations showed full width half maxima (FWHM) ranging between 0.05° and 0.08°. The
119 unit-cell lattice parameters were determined by vector least-square fitting of 22 reflections, each centered
120 in 8-positions (King and Finger 1979; Ralph and Finger 1982) yielding the following unit-cell lattice
121 parameters: $a = 4.74653(13) \text{ \AA}$, $c = 4.29002(19) \text{ \AA}$ and $V = 83.703(6) \text{ \AA}^3$. Intensity data for the same

crystal were collected on a Xcalibur diffractometer (Rigaku, Oxford Diffraction) equipped with a Sapphire2 CCD detector and graphite-monochromatized MoK α radiation operated at 50 kV and 40 mA. X-ray scans were acquired upon ω -rotations of the crystal up to $2\theta_{\max} = 90^\circ$ with exposure times of 5 s or 15 s at low and high 2θ , respectively. *CrisAllysPro* (Rigaku, Oxford Diffraction) was used for data processing, which included integration of intensities, correction for Lorentz and polarization factors, frame scaling and empirical absorption correction based on spherical harmonics. The obtained average redundancy of unique reflections was 6.2 in the Laue class $\bar{3}m$. The space groups $P6_3$, $P6_3/m$ and $P6_322$ resulted compatible with the analysis of systematic absences. In addition, we also tested a structural model having space group $P\bar{3}1m$, i.e. the same as Mg-Phase D. No evidence for polytypism along the c^* axis was found through the analysis of unwarp images of reciprocal planes $h0l$ and $h1l$. However, strong diffuse scattering was observed in the $hk1$, $hk3$, etc. reciprocal planes (Figure 2), as discussed later. For the hexagonal space groups, structure solutions were performed using the dual-space algorithm *SHELXT* (Sheldrick 2015b) and the structural model was refined based on F^2 using *SHELXL* (Sheldrick 2015a) in the *ShelXle* GUI (Hübschle et al. 2011). As Al-phase D has only partially occupied cationic sites, in our structural refinement we assumed Al, Si and Fe to be completely disordered in each site and their cation fractions to be $X_{\text{Al}} : X_{\text{Si}} : X_{\text{Fe}} = 0.59 : 0.33 : 0.08$, as determined by EPMA. The total occupancy of each site was then refined independently. Mean atomic numbers (m.a.n.) for each site were finally calculated by multiplying the site occupancy factors obtained in our structural models by the fraction X_i of each cation ($i = \text{Al, Si, Fe}$) and its atomic number. In their final cycles, structural refinements for all space groups resulted in discrepancy factors (R1) not exceeding 5.1%, with the exception of $P6_3/m$ (R1 > 20%). Further details on the structural models with space groups $P6_322$ and $P\bar{3}1m$ are provided in the deposited Crystallographic Information File (CIF). An attempt was also made for the $P6_322$ space group to refine the distribution of cations among the different crystallographic sites without constraining the cation

fraction but simply using restraints on the chemical composition, in order to shed light on potential order of Fe vs Al + Si. However, due to the lack of information on the total occupancy of the sites, which are only partially occupied, the model resulted less stable than the one described above, showing an increased $R1 = 8.6\%$ and negative occupancy factors for some of the sites. Therefore, this structural model was discarded.

Single-crystal X-ray diffraction at high pressure

In order to study the compressibility of Fe-bearing Al-phase D, we performed single-crystal X-ray diffraction measurements in DAC up to ~ 52 GPa at the Extreme Conditions Beamline (ECB) P02.2 of PETRA III (Hamburg, Germany). Two runs were performed using either $8 \times 3 \mu\text{m}^2$ or $2 \times 2 \mu\text{m}^2$ (FWHM) X-ray beams of 25.6 and 42.7 keV respectively, and a Perkin-Elmer XRD 1621 flat panel detector (Liermann et al. 2015). The sample-detector distance was calibrated using polycrystalline CeO_2 and the instrument parameters for single-crystal X-ray diffraction were refined using a natural enstatite standard. To generate high pressures, BX-90 type DACs capable to provide opening angles of up to 90° (Kantor et al. 2012) were employed together with Almax-Boehler diamonds (Boehler and De Hantsetters 2004) having culets of $350 \mu\text{m}$ (run 1) or $250 \mu\text{m}$ (run 2) in diameter and WC seats with large ($\sim 80^\circ$) opening angle. According to the target pressure of each run, i.e. ~ 38 GPa in run 1 and 52 GPa in run 2, a Re gasket was indented to 53 or 35 μm , respectively, and laser-drilled to create the sample chamber. The same high-quality single-crystal of Fe-bearing Al-phase D of approximately $20 \times 10 \times 10 \mu\text{m}^3$ was employed for both runs. A ruby sphere serving as pressure standard (Shen et al. 2020) and a piece of Au for fine alignment of the DAC under the X-ray beam were also placed in the sample chambers next to the crystal. Pre-compressed He at 0.13 GPa was loaded as quasi-hydrostatic pressure transmitting medium in both runs using the gas loading system installed at the Bayerisches Geoinstitut, University of Bayreuth (Kurnosov et al. 2008). Pressure was increased online using a gas-driven membrane up to about 38 GPa (run 1) and

168 52 GPa (run 2) with steps of 2-4 GPa. X-ray scans were collected upon continuous omega rotation of the
169 DAC between -35° and $+35^{\circ}$, with steps of 0.5° and an exposure time of 1 s. Data analysis was performed
170 using *CrisAllysPro* (Rigaku, Oxford Diffraction) following the same procedure described for *in-house*
171 measurements at room pressure. In addition to high-pressure measurements, another single-crystal grain
172 with a diameter of less than 20 μm was also measured at ambient conditions at the same beamline to
173 analyze its crystal structure. To do so, the crystal was placed on the culet of a DAC without loading (i.e.,
174 the crystal was still at room pressure) and intensity data were collected following the same procedure
175 employed for high-pressure measurements and described above. The measured unit-cell lattice parameters
176 for this crystal are $a = 4.7469(4) \text{ \AA}$, $c = 4.2891(6) \text{ \AA}$, and $V = 83.698(17) \text{ \AA}^3$, in very good agreement with
177 *in-house* measurements. Further information can be found in the deposited CIF.

178 **Results and discussion**

179 **Crystal structure of Fe-bearing Al-Phase D**

180 Three of the four structural models that were tested in this study, i.e. $P\bar{3}1m$, $P6_3$ and $P6_322$, yielded
181 discrepancy factors (R1) of 5% or less. Models having $P6_3$ and $P6_322$ space group symmetries resulted
182 identical to each other within uncertainties in terms of both atomic positions and site occupancy factors.
183 Therefore, only the higher symmetry space group $P6_322$ will be discussed as it employs a smaller number
184 of refined parameters. In Mg-bearing Al-phase D ($P\bar{3}1m$ space group) analyzed by Boffa Ballaran et al.
185 (2010), mean atomic numbers (m.a.n.) were calculated by allowing the site occupancy factor (s.o.f.) of a
186 given site to be refined and subsequently multiplying the s.o.f. by the number of electrons of the scattering
187 factors (for Si or Al) used to refine the occupancy at a given site. In this way, it was possible to quantify
188 the amount of charge present in the M1, M2, and M3 sites of their phase D sample independently of the
189 atomic species (i.e., Mg, Al, Si, or Fe) which were actually present at that site. Boffa Ballaran et al. (2010)

190 found in that way that the m.a.n. of M2 is larger than that of M3, i.e. the adjacent octahedral site that shares
191 faces with M2 perpendicular to the *c*-axis (Supplementary Figure S1a). The cation distribution in their
192 sample indicates that within a given unit cell there is a higher probability that Si and Al atoms occupy
193 edge sharing octahedra on the same interstitial layer rather than face-sharing sites on adjacent layers. Such
194 mechanism seems to change, however, in the Fe-bearing Al-phase D sample analyzed in this study, as in
195 both the $P\bar{3}1m$ and $P6_322$ space groups, all the cationic sites resulted to be partially occupied and with
196 different m.a.n. It follows that our Fe-bearing Al-phase D (Supplementary Figure S1c) represents an
197 intermediate configuration between those of Mg-bearing (Supplementary Figure S1a) and Fe-free Al-
198 phase D (Supplementary Figure S1b), where all sites are equally populated and with almost identical
199 m.a.n.

200 The main differences between the $P\bar{3}1m$ and $P6_322$ models analyzed here consist of: (i) a shift in
201 the origin of the unit cell of the $P6_322$ model by $(1/3, 1/3, 1/4)$ with respect to that of the $P\bar{3}1m$ model and
202 (ii) an apparently different distribution of the cations over the four crystallographic sites, resulting from
203 different site occupancy factors and point group symmetry at the cation sites. In the trigonal model, the
204 face-sharing octahedral sites M2 and M3 (Supplementary Figure S1a) exhibit m.a.n. of 8.10(7) and 4.27(5)
205 respectively, while M1 and M4, which are also face-sharing, have m.a.n. equal to 9.71(8) and 2.50(7). In
206 the space group $P6_322$, on the other hand, only three distinct cation sites exist (Supplementary Figure
207 S1c). The first site has Wyckoff position 2b and its symmetry-equivalent coordinates are $(0, 0, 1/4)$ and
208 $(0, 0, 3/4)$, resulting in a chain of equivalent face-sharing octahedra aligned along the *c*-axis
209 (Supplementary Figure S1c). The m.a.n. of the 2b site is 6.23(7), meaning that its occupancy factor is
210 about 43%. The other two sites have Wyckoff positions 2c and 2d and occupy the two remaining
211 octahedral sites. These two sites lie at $x = 1/3, y = 2/3$ and $x = 2/3, y = 1/3$ of each interstitial layer, with
212 their *x* and *y* coordinates swapping every interstitial layer. This means that in the first layer, where $z = 1/4$,

213 2c lies at (1/3, 2/3, 1/4) and 2d at (2/3, 1/3, 1/4), while in the second layer, having $z = 3/4$, 2c is located at
214 (2/3, 1/3, 3/4) and 2d at (1/3, 2/3, 3/4). In other words, 2c octahedra share edges with 2d octahedra that
215 are in the same interstitial layer and faces with 2d octahedra lying on adjacent layers, and vice versa
216 (Supplementary Figure S1c). The m.a.n. refined for the 2c and 2d sites are 2.99(8) and 9.33(9),
217 respectively, which correspond to site occupancy factors of about 21% and 65%, respectively. This
218 configuration differs from that of Mg-bearing Al-phase D (Boffa Ballaran et al. 2010), where M2 and M3
219 sites are located on different interstitial layers (Supplementary Figure S1a) and may occur because of the
220 smaller ionic radius of Fe^{3+} relative to Mg^{2+} , which favors cation mixing. For comparison, we determined
221 the m.a.n. of the cation sites in the space group $P6_322$ for the sample measured at ambient conditions at
222 the ECB P02.2 and obtained values of 6.36(7), 3.58(7) and 9.19(12) for 2b, 2c and 2d, respectively, which
223 are in good agreement with those determined from *in-house* measurements. The total number of Al, Si
224 and Fe cations for 6 oxygens calculated from the site occupancy factors determined from *in-house* and
225 synchrotron data falls within a $\pm 2\%$ interval relative to that determined by EPMA. The m.a.n. of the 2b
226 and 2d sites in the two samples are the same within mutual uncertainties, while that of 2c is higher in the
227 sample measured at the ECB P02.2. This could indicate, for instance, that the degree of cation disordering
228 in the two samples is slightly different.

229 Hamilton (1965) proposed a statistical test to assess whether the increase in the number of
230 parameters between similar structural models produces a statistically significant improvement in the
231 quality of the structural refinement. One condition to apply Hamilton's test is that the number of unique
232 reflections in the two structural models is the same. This condition is not fulfilled by the space groups
233 $P6_322$ and $P\bar{3}1m$ since they belong to different Laue classes and thus have different averaging rules. If the
234 test is conducted while neglecting this condition, the hypothesis that the hexagonal model better represents
235 the actual atomic configuration is rejected at a 0.005 significance level, meaning that the trigonal model

should be used. A way to properly apply Hamilton's test would be to compare the hexagonal and trigonal structural models refined against non-merged datasets. In this case, the number of reflections is the same by definition as long as the reflection file in the two refinements is the same. This procedure yielded a slightly larger weighted R factor for the $P\bar{3}1m$ model relatively to the $P6_322$ model. Therefore, in the case of non-merged intensities, the hypothesis that the hexagonal model better represents the actual atomic configuration cannot be rejected. The apparent contradiction between the two approaches to Hamilton's test prevents us from drawing any conclusion on which model is the most suitable to describe the structure of Fe-bearing Al-phase D.

Like previously analyzed Al-rich phase D samples, we observed no long-range octahedral distortion, with M-O distances being all identical to each other within uncertainties. As pointed out by Boffa Ballaran et al. (2010), this does not exclude that distortions can arise at the local scale due to the fact that in each given unit cell only three of the six cationic sites must be occupied so that charge balance is preserved. Boffa Ballaran et al. (2010) ruled out the possibility of cation ordering in their Mg-bearing Al-phase D sample due to absence of additional peaks in the X-ray diffraction scans that would indicate the presence of a superstructure. However, weak diffuse scattering was observed in electron diffraction images, suggesting that short range ordering of the cations might exist at the nanoscale. Our Fe-bearing Al-phase D sample, on the other hand, shows much stronger diffuse scattering streaks that are well visible in X-ray diffraction images. Unwarps obtained by integration of X-ray scans collected both *in-house* and at the beamline P02.2 show that diffuse scattering is localized in reciprocal planes having odd l indices and only between reflections that satisfy the conditions $h-k=3n+1$ or $h-k=3n+2$, where n is an integer number (Figure 2). If we consider the space group $P6_322$, the first condition rules out any influence of the cation site 2b, for which the existence condition of any hkl reflection is $l=2n$. When $h-k=3n$ and $l=2n+1$, i.e. when the contribution of Wyckoff positions 2c and 2d to the structure factor is null, no diffuse

scattering streaks are observed around the peaks. Therefore, diffuse scattering must originate from the short-range ordering of cations in 2c and 2d. On the other hand, in the trigonal space group $P\bar{3}1m$, there is no extinction rule for any atomic position due to the absence of additional translational symmetry. Therefore, it would be difficult to reconcile such a peculiar type of diffuse scattering with partial ordering of cations over the four available octahedral sites of the trigonal structure. Our analysis of diffuse scattering thus suggests that the hexagonal space group is more suitable to describe the crystal structure and partial ordering of Fe-bearing Al-phase D. Owing to the difference in wavelength between *in-house* and synchrotron experiments, the types of diffuse scattering observed in the diffraction patterns have slightly different features, as short wavelengths can probe displacements at higher resolution. In fact, in the unwarps from synchrotron measurements, homogeneous streaks are found to connect the main reflections (Figure 2d), while weak additional peaks appear at 1/2 or 1/3 fractional positions between the main reflections in the unwarps obtained from *in-house* measurements (Figure 2b).

From our structural model, the bond valence analysis of oxygen atoms can also be performed following the example of Pamato et al. (2015). We employed the computer software SPuDS (Lufaso and Woodward 2001) to compute the effective charge of each bond using the interatomic distances and site occupancy factors for each cation site that were obtained from our structural models. Note that because Al, Si and Fe coexist in the same crystallographic sites, the contribution of each cation to the bond valence was weighted by their abundances, X_i , with $i = \text{Al, Si, Fe}$. We obtained an effective Pauling bond strength of +1.42 from both the $P\bar{3}1m$ and $P6_322$ models, which is identical to that determined for Al-phase D (Pamato et al., 2015) and larger than Mg-rich compositions (Yang et al. 1997; Boffa Ballaran et al. 2010), supporting the hypothesis that cation disordering seems to induce stronger H bonds. In Mg-phase D, H-bonds are oriented along the edges of the vacant octahedral sites M3 and M4 (Supplementary Figure S1a) and their respective O···O distance is 2.675 Å (Yang et al. 1997). The O···O distance measured along the

edges of octahedra of pure Al-phase D is 2.655(3) Å (Pamato et al. 2015), while for Fe-bearing Al-phase D it is 2.665(1) Å, which are both smaller than in Mg-phase D since the spacing between O layer stacked perpendicular to the *c*-axis is smaller. For comparison, O···O distances at ambient conditions in phase H and phase δ -AlOOH are 2.461(4) and 2.5479(12) Å, respectively. Phase δ is known to undergo H-bond disordering, followed by symmetrization, only when the O···O distances drop below the critical value of 2.443 Å (Meier et al. 2022). Therefore, it is unlikely that H-bonds in Al-phase D samples are symmetric, as they are about 4% larger than phase δ and 9% larger than the critical value of 2.443 Å.

Equation of state of Fe-bearing Al-phase D

The evolution of the unit-cell volume and lattice parameters of Fe-bearing Al-phase D (Table 1) is displayed in Figure 3. A slight change in slope of the volume variation with pressure is observed above 38 GPa. For this reason the volume compression of Fe-bearing Al-phase D has been first obtained between room pressure and 38 GPa, by fitting the pressure-volume (*P*-*V*) data set to both a 3rd-order Birch-Murnaghan (BM3) (Birch 1947) and a Vinet (Vinet et al. 1989) equation of state (EOS). Following a similar approach, we use linearized BM3 and Vinet equations of state to fit the pressure evolution of individual unit-cell parameters (*l*) of Fe-bearing Al-phase D, where *V* was substituted by the cube of the unit cell parameters (*l*³), $3K_{T0}$ by the axial modulus M_{l0} and $3K'_{T0}$ by the axial modulus pressure derivative M'_{l0} (Angel 2000; Angel et al. 2014). Fitting was performed using the EosFit7c library implemented in EosFit7-GUI (Angel et al. 2014; Gonzalez-Platas et al. 2016) and fitting parameters are reported in Table 2. The EOS parameters values obtained from the two equation of states formalisms are identical within their mutual uncertainties (Table 2) resulting in volume and linear EOSs perfectly overlapping in the pressure range considered (i.e., 0.0001-38 GPa). Therefore, for clarity, only the curves derived from the BM3 fits are shown in Figure 3. Moreover, the fitted V_0 is in very good agreement with the unit-cell volume measured *in-house* and the beamline P02.2 at room pressure. Consistently with previous

observations on Mg-rich phase D in this pressure range, we observe that the a -axis is more compressible than the c -axis (Table 2), despite the difference between the two axial moduli ($M_{a0} = 539$ GPa and $M_{c0} = 421$ GPa) being smaller than in Mg-phase D ($M_{a0} = 546$ -669 GPa and $M_{c0} = 322$ -326 GPa) (Rosa et al. 2013; Wu et al. 2016) and Fe,Al-bearing Mg-phase D by ($M_{a0} = 545$ -634 GPa and $M_{c0} = 216$ -326 GPa) (Chang et al., 2013; Wu et al., 2016). In fact, although the room pressure value of the c/a ratio for Fe-bearing Al-phase D is similar to those reported in previous studies for Fe-bearing Mg-phase D samples, this changes by only 0.8% upon compression from room pressure to 38 GPa (0.904 to 0.897), which is much less than values of ~2.2% and ~3.3% determined for pure and Fe-bearing Mg-phase D, respectively (Frost and Fei 1999; Litasov et al. 2008; Hushur et al. 2011; Chang et al. 2013; Rosa et al. 2013; Wu et al. 2016). A possible reason for these two different behaviors is that all cation sites in Al-phase D are at least partially occupied and are geometrically more regular than in Mg-phase D (Supplementary Figure S1b-c), which can lead to a less anisotropic compression mechanism of the two interstitial layers relative to Mg-rich compositions, where nominally vacant sites exist, and Mg and Si cations occupy different layers (Supplementary Figure S1a).

A large number of experimental studies aimed at constraining the compression behavior of pure and Fe,Al-bearing Mg-phase D (Table 3, Supplementary Figure S2). Our results show that the bulk modulus of Fe-bearing Al-phase D falls toward the higher boundary of the range of values proposed for Mg-phase D (143-168 GPa, Frost and Fei 1999; Hushur et al. 2011; Rosa et al. 2012, 2013). Only one study (Wu et al. 2016) reports a much higher bulk modulus of 179(1) GPa, which is likely related to the use of a 2nd-order BM EOS (i.e. $K'_{T0} = 4$) to fit the data. In contrast, all other studies suggest that Mg-phase D, as well as Fe-bearing Mg-phase D have a first pressure derivative larger than 4. The lower values of K_{T0} for Mg-phase D are confirmed by a single crystal X-ray diffraction study (Rosa et al., 2013) and a single-crystal Brillouin scattering study (Rosa et al., 2012) on Mg-Phase D samples with very similar

compositions that reported consistent values of $K_{T0} = 151(1)$ and $K_{T0} = 149(3)$ GPa, respectively. Xu et al. (2020) recently determined the pressure and temperature dependence of the sound velocities of Al-bearing Mg-phase D by ultrasonic interferometry and synchrotron X-ray powder diffraction, suggesting that Al incorporation in phase D decreases the bulk modulus of Mg-phase D at ambient conditions. Note, however, that when the tradeoff between K_{T0} and K'_{T0} is taken into account, the range of values determined for phase D in previous studies (Litasov et al. 2007, 2008; Chang et al. 2013; Rosa et al. 2013; Wu et al. 2016; Xu et al. 2020) falls in a relatively narrow range (Supplementary Figure S2). As a consequence, the range of K_T values becomes inevitably smaller with increasing pressure and results in a much weaker compositional effect on the elasticity of phase D solid solutions at mantle transition zone and lower mantle pressures.

Spin crossover in Fe-bearing Al-phase D

When Fe^{2+} and/or Fe^{3+} are incorporated in phase D, they are known to undergo a high-spin (HS) to low-spin (LS) crossover in the pressure interval ranging between 40 and 65 GPa, as revealed by X-ray emission spectroscopy (XES) (Chang et al. 2013) and synchrotron Mössbauer spectroscopy (SMS) (Wu et al. 2016) observations. Wu et al. (2016) determined that the fraction of Fe^{2+} present in their sample is about 60%, corresponding to 0.07 Fe^{2+} atoms per formula unit, which is believed to induce the sharp volume collapse of 1.7% observed by X-ray diffraction in a few GPa interval at about 40 GPa. A second drop in the unit-cell volume (2%) at about 65 GPa was linked to the spin crossover of Fe^{3+} also present in the sample. On the other hand, Chang et al. (2013) analyzed a phase D sample having less than 0.01 Fe^{2+} per formula unit and observed a smooth continuous decrease both in the unit-cell volume by X-ray diffraction and in the Fe^{3+} high-spin component by XES from 40 to 70 GPa. In this study, we observed a smooth and progressive deviation of the unit-cell volume, V , and lattice parameters a and c from the extrapolation of their respective equations of state determined using the data up to 38 GPa, i.e. below the

region at which spin crossover may occur. Owing to the similar $\text{Fe}^{3+}/\Sigma\text{Fe}$ ratio of our Fe-bearing Al-phase D with that of the sample studied by Chang et al. (2013), we also interpret the volume decrease above 38 GPa as the onset of Fe^{3+} spin crossover, suggesting that the $\text{Mg}^{2+} + \text{Si}^{4+} = 2\text{Al}^{3+}$ substitution has little to no effect on the spin crossover pressure of Fe^{3+} in phase D.

The number of data points collected after the onset of the spin crossover (i.e. above 38 GPa) is limited and does not allow to refine separate EOS parameters for the Fe-bearing Al-phase D sample in the high- and low-spin states. However, a fit of all data points (i.e. before and across the spin crossover) can be obtained using a new semi-empirical formalism that has been recently proposed by Buchen (2021). In this formalism, the contribution of the spin crossover to the elastic energy (and thus to pressure) is obtained from the volume dependency of crystal-field parameters such as the crystal-field splitting Δ and the Racah parameters B and C :

$$\Delta = \Delta_0 \left(\frac{V_0}{V} \right)^{\frac{\delta}{3}}, \quad B = B_0 \left(\frac{V_0}{V} \right)^{\frac{b}{3}}, \quad C = C_0 \left(\frac{V_0}{V} \right)^{\frac{c}{3}} \quad (1)$$

where the zero in the subscript denotes parameters at room pressure. The total Helmholtz free energy (F) at a given volume is then calculated by summing the elastic energy obtained from the finite strain equation (i.e., BM3 EOS in this case), the energies associated with the three most populated electronic states (i.e., ${}^6\text{A}_1$, ${}^2\text{T}_2$, ${}^4\text{T}_1$ for Fe^{3+}) according to the equations proposed by Tanabe and Sugano (1954), and a term accounting for configurational entropy. Finally, pressure is calculated by differentiating the total Helmholtz free energy relative to volume as $P = -(\partial F / \partial V)$. This strategy has the advantage that only one set of V_0 , $K_{\text{T}0}$, and $K'_{\text{T}0}$ needs to be determined for the high-spin state, the low spin state, and the mixed-spin region, while the electronic contribution to the spin-crossover equation is calculated separately. Buchen (2021) further showed that a good fit to the experimentally measured P - V data can be obtained even when most of these parameters, such as Δ_0 , b , and c , are fixed to values determined by

373 previous studies for octahedrally coordinated Fe^{2+} and Fe^{3+} cations in other compounds, while only B_0 and
374 δ are refined. Following the examples provided by Buchen (2021), we assumed C/B to be constant and
375 equal to 4.73, which implies $c = b$, with $b = -2$ (as Fe^{3+} in CF-type aluminous phase, Buchen 2021) and Δ_0
376 $= 14750 \text{ cm}^{-1}$ (as Fe^{3+} in corundum, Lehmann and Harder 1970; Krebs and Maisch 1971), while B_0 and δ
377 were refined. The resulting fit parameters are reported in Table 2 and the fit to the experimental data points
378 is shown in Figure 3a. The EOS curve interpolates well the data points in both the high-spin state region
379 and across the spin crossover, while the population density of the high-spin and low-spin electronic states,
380 shown in the inset of Figure 3a, confirms that the transition is broad and takes place over a pressure interval
381 of more than 30 GPa, as was previously observed by Chang et al. (2013). Note also that the room pressure
382 values V_0 , K_{T0} and K'_{T0} obtained from this fit are in agreement with the values obtained fitting the P - V
383 data only up to 38 GPa (Table 2) once the tradeoff between K_{T0} and K'_{T0} is taken into account, confirming
384 the validity of the formalism used.

385 In Fe-bearing Mg-phase D, the volume drop at the spin crossover is mainly driven by a shrinking of the c
386 lattice parameter, whereas the a lattice parameter remains almost unaffected (Chang et al. 2013; Wu et al.
387 2016). In Fe-bearing Al-phase D, on the other hand, we observe a smooth decrease of both the a and c
388 axes, with the c/a ratio remaining almost constant across the spin crossover (Figure 3b). The reason behind
389 the different behavior shown by our sample relative to previous studies could be that, in Mg-phase D,
390 ferric and ferrous Fe likely substitute Mg in the M1 site and not Si in the M2 site. As described above, in
391 Mg-phase D the distance between oxygen atoms across the interstitial layer hosting M1 is larger than that
392 across M2, owing to the larger radius of Mg relative to Si (Supplementary Figure S1a). In order to
393 accommodate the difference in size of the two cations, the z coordinates of O in Mg-Phase D (Wyckoff
394 position 6k: $x,0,z$) are either larger than 1/4 or smaller than 3/4, making the Si layer thinner than the Mg
395 layer (Supplementary Figure S1a). At the spin crossover, the ionic radius of Fe decreases and thus the

octahedral volume of M1 in Mg-phase D must decrease as well. This means that in order for M1 to be reduced in size while leaving M2 unaffected, the c lattice parameter must shrink while the z coordinates of O approaches the value 1/4 or 3/4. In Fe-bearing Al-phase D, this cannot happen when the hexagonal space group is considered, since the z coordinate of the oxygen atoms is constrained by symmetry (Wyckoff position 6g: $x,x,1/2$) and the two interstitial layers perpendicular to the c -axis have the same thickness. This is likely the consequence of Al, Si and Fe^{3+} being more or less randomly distributed in Fe-bearing Al-phase D (Supplementary Figure S1c). Therefore, the octahedral volumes of the three cation sites must collapse simultaneously while the atomic coordinates of all atoms are likely to remain unchanged. The fact that we observed a simultaneous decrease of the a and c lattice parameters above 38 GPa seems to confirm indeed the hypothesis of a hexagonal space group for our sample.

Recently, Meier et al. (2022) analyzed the possible correlations between H-bond symmetrization and high-to-low spin crossover in Fe-bearing phase δ and Fe,Al-bearing Mg-phase D by means of nuclear magnetic resonance spectroscopy (NMR), synchrotron Mössbauer spectroscopy, and X-ray diffraction. In all the samples studied by Meier et al. (2022), including the one of Fe,Al-bearing Mg-phase D, the H-bond symmetrization was found not to affect the resonance frequency of the ^1H nuclei, but only the width of the peak, which is related to the proton mobility. The spin crossover of Fe^{3+} , on the other hand, was found to significantly change the resonance frequency of the ^1H , while leaving the width of the NMR signal unaffected. These two phenomena were observed at different pressures in all the hydrous phases investigated by Meier et al. (2022), suggesting that they are not correlated. The H-bond symmetrization in the phase D sample was observed at 23(2) GPa, while the spin crossover of Fe^{3+} was observed above 36 GPa, which is in good agreement with both our observations and the previous study of Chang et al. (2013). As the strength of H-bonds in Al-phase D samples is higher than in Mg-phase D samples (Yang et al. 1997; Boffa Ballaran et al. 2010; Pamato et al. 2015), it is reasonable to expect that the

symmetrization of H-bond in Al-phase D will take place at lower pressure than in Mg-phase D. Therefore, we expect that the H-bond symmetrization and spin crossover of Fe^{3+} in Fe-bearing Al-phase D are uncorrelated, similarly to what was observed in Fe,Al-bearing Mg-phase D by Meier et al. (2022).

Implications

Previous experimental studies have shown that the wide P - T stability field of phase D makes it a suitable host for water in the Earth's mantle transition zone and lower mantle (Nishi et al. 2014; Pamato et al. 2015; Liu et al. 2019). As Al is incorporated in its crystal structure, phase D can survive even at temperatures of the ambient mantle within MgO-poor Al-rich subducted basaltic crust, where water can be delivered by hydrous melts upwelling from dehydrating ultramafic lithologies within the slab (Pamato et al. 2015). Al-rich phase D was also reported to be stable in MgO-rich basaltic crust between 20 and 25 GPa (Liu et al. 2019) and to transform to a solid solution of δ - AlOOH and DHMS phase H (MgSiO_4H_2) above 25 GPa. It was recently proposed that solid solutions between phase H and δ - AlOOH contribute to make the sound velocities of hydrous mid-ocean ridge basalt (MORB) faster than those of dry MORB at shallow lower mantle pressures, owing to their high bulk modulus and relative low density after the H-bond symmetrization (Satta et al. 2021). These findings are particularly interesting as they suggest an intimate relation between H-bond symmetrization and elastic stiffening of CaCl_2 -type oxyhydroxides at high pressure. Based on the analysis of bond valences and Pauling bond strength of our sample and that studied by Pamato et al. (2015), it seems that the H-bonds of Al-Phase D are stronger than those of Mg-phase D. Nuclear magnetic resonance (NMR) spectroscopy and single-crystal diffraction measurements on a Fe,Al-bearing Mg-phase D sample, however, showed no evidence for a shift in the resonance

441 frequency and a change in compressibility across the H-bond symmetrization (Meier et al., 2022). Given
442 that the H-bonds in Al-phase D and Fe-bearing Al-phase D are stronger than in Mg-phase D samples, it is
443 reasonable to expect the H-bond symmetrization to take place below 23 GPa. However, no change in the
444 volume and axial compressibility was observed in Fe-bearing Al-phase D between room pressure and 38
445 GPa. Therefore, we conclude that the strength of H-bonds alone cannot be responsible for an increase in
446 the bulk modulus of phase D and other H-bearing minerals, but additional features, such as a change in
447 the space group symmetry, must also occur across the H-bond symmetrization, as it was observed in the
448 case of pure and Fe-bearing phase δ (Sano-Furukawa et al. 2018; Ohira et al. 2019; Satta et al. 2021).

449

450 **Acknowledgments**

451 We like to thank Raphael Njul for preparing the samples for EPMA and Detlef Krauß for his assistance
452 with EPMA measurements. Johannes Buchen is acknowledged for fruitful discussion on the spin-
453 crossover equation of state and for sharing the script to fit the P - V data. We also thank Oliver Tschauner,
454 Angelika D. Rosa, and an anonymous reviewer for their constructive comments that helped us improving
455 the manuscript. We acknowledge DESY (Hamburg, Germany), a member of the Helmholtz Association
456 HGF, for the provision of experimental facilities. Parts of this research were carried out at the Extreme
457 Conditions Beamline P02.2, PETRA-III.

458 **References**

- 459 Angel, R.J. (2000) Equations of State. *Reviews in Mineralogy and Geochemistry*, 41, 35–59.
- 460 Angel, R.J., and Finger, L.W. (2011) SINGLE: A program to control single-crystal diffractometers.
461 *Journal of Applied Crystallography*, 44, 247–251.
- 462 Angel, R.J., Gonzalez-Platas, J., and Alvaro, M. (2014) EosFit7c and a Fortran module (library) for
463 equation of state calculations. *Zeitschrift fur Kristallographie*, 229, 405–419.
- 464 Bindi, L., Nishi, M., Tsuchiya, J., and Irifune, T. (2014) Crystal chemistry of dense hydrous magnesium
465 silicates : The structure of phase H , 99, 1802–1805.
- 466 Birch, F. (1947) Finite elastic strain of cubic crystals. *Physical Review*, 71, 809–824.
- 467 Boehler, R., and De Hantsetters, K. (2004) New anvil designs in diamond-cells. *High Pressure Research*,
468 24, 391–396.
- 469 Boffa Ballaran, T., Frost, D.J., Miyajima, N., and Heidelblbach, F. (2010) The structure of a super-
470 aluminous version of the dense hydrous-magnesium silicate phase D. *American Mineralogist*, 95,
471 1113–1116.
- 472 Buchen, J. (2021) Seismic Wave Velocities in Earth’s Mantle from Mineral Elasticity, 51–95 p. *Mantle*
473 *Convection and Surface Expressions*.
- 474 Chang, Y.Y., Jacobsen, S.D., Lin, J.F., Bina, C.R., Thomas, S.M., Wu, J., Shen, G., Xiao, Y., Chow, P.,
475 Frost, D.J., and others (2013) Spin transition of Fe³⁺ in Al-bearing phase D: An alternative
476 explanation for small-scale seismic scatterers in the mid-lower mantle. *Earth and Planetary Science*
477 *Letters*, 382, 1–9.

- 478 Frost, D.J. (2006) The Stability of Hydrous Mantle Phases. *Reviews in Mineralogy and Geochemistry*,
479 62, 243–271.
- 480 Frost, D.J., and Fei, Y. (1999) Static compression of the hydrous magnesium silicate phase D to 30 GPa
481 at room temperature. *Physics and Chemistry of Minerals*, 26, 415–418.
- 482 Gonzalez-Platas, J., Alvaro, M., Nestola, F., and Angel, R.J. (2016) EosFit7-GUI: A new graphical user
483 interface for equation of state calculations, analyses and teaching. *Journal of Applied*
484 *Crystallography*, 49, 1377–1382.
- 485 Hamilton, W.C. (1965) Significance tests on the crystallographic R factor . *Acta Crystallographica*, 18,
486 502–510.
- 487 Hübschle, C.B., Sheldrick, G.M., and Dittrich, B. (2011) ShelXle: A Qt graphical user interface for
488 SHELXL. *Journal of Applied Crystallography*, 44, 1281–1284.
- 489 Hushur, A., Manghnani, M.H., Smyth, J.R., Williams, Q., Hellebrand, E., Lonappan, D., Ye, Y., Dera,
490 P., and Frost, D.J. (2011) Hydrogen bond symmetrization and equation of state of phase D. *Journal*
491 *of Geophysical Research: Solid Earth*, 116, 1–8.
- 492 Ishii, T., Shi, L., Huang, R., Tsujino, N., Druzhbin, D., Myhill, R., Li, Y., Wang, L., Yamamoto, T.,
493 Miyajima, N., and others (2016) Generation of pressures over 40 GPa using Kawai-type multi-anvil
494 press with tungsten carbide anvils. *Review of Scientific Instruments*, 87.
- 495 Ishii, T., Liu, Z., and Katsura, T. (2019) A Breakthrough in Pressure Generation by a Kawai-Type
496 Multi-Anvil Apparatus with Tungsten Carbide Anvils. *Engineering*, 5, 434–440.
- 497 Kantor, I., Prakapenka, V., Kantor, A., Dera, P., Kurnosov, A., Sinogeikin, S., Dubrovinskaia, N., and
498 Dubrovinsky, L. (2012) BX90: A new diamond anvil cell design for X-ray diffraction and optical

- 499 measurements. *Review of Scientific Instruments*, 83, 125102.
- 500 King, H.E., and Finger, L.W. (1979) Diffracted beam crystal centering and its application to high-
501 pressure crystallography. *Journal of Applied Crystallography*, 12, 374–378.
- 502 Krebs, J.J., and Maisch, W.G. (1971) Study of pure and doped cobaltous and nickelous oxide. *Physical*
503 *Review B*, 4, 750–757.
- 504 Kurnosov, A., Kantor, I., Boffa-Ballaran, T., Lindhardt, S., Dubrovinsky, L., Kuznetsov, A., and
505 Zehnder, B.H. (2008) A novel gas-loading system for mechanically closing of various types of
506 diamond anvil cells. *Review of Scientific Instruments*, 79, 045110.
- 507 Lehmann, G., and Harder, H. (1970) Optical Spectra of Di- and Trivalent Iron in Corundum. *American*
508 *Mineralogist*, 55, 98–105.
- 509 Liermann, H.P., Konôpková, Z., Morgenroth, W., Glazyrin, K., Bednarčík, J., McBride, E.E.,
510 Petitgirard, S., Delitz, J.T., Wendt, M., Bican, Y., and others (2015) The Extreme Conditions
511 Beamline P02.2 and the Extreme Conditions Science Infrastructure at PETRA III. *Journal of*
512 *Synchrotron Radiation*, 22, 908–924.
- 513 Litasov, K.D., Ohtani, E., Suzuki, A., and Funakoshi, K. (2007) The compressibility of Fe- and Al-
514 bearing phase D to 30 GPa. *Physics and Chemistry of Minerals*, 34, 159–167.
- 515 Litasov, K.D., Ohtani, E., Nishihara, Y., Suzuki, A., and Funakoshi, K. (2008) Thermal equation of state
516 of Al- and Fe-bearing phase D. *Journal of Geophysical Research: Solid Earth*, 113, 1–13.
- 517 Liu, X., Matsukage, K.N., Nishihara, Y., Suzuki, T., and Takahashi, E. (2019) Stability of the hydrous
518 phases of Al-rich phase D and Al-rich phase H in deep subducted oceanic crust. *American*
519 *Mineralogist*, 104, 64–72.

- 520 Liu, Z., Nishi, M., Ishii, T., Fei, H., Miyajima, N., Ballaran, T.B., Ohfuji, H., Sakai, T., Wang, L.,
521 Shcheka, S., and others (2017) Phase Relations in the System $\text{MgSiO}_3\text{-Al}_2\text{O}_3$ up to 2300 K at
522 Lower Mantle Pressures. *Journal of Geophysical Research: Solid Earth*, 122, 7775–7788.
- 523 Lufaso, M.W., and Woodward, P.M. (2001) Prediction of the crystal structures of perovskites using the
524 software program SPuDS. *Acta Crystallographica Section B: Structural Science*, 57, 725–738.
- 525 McCammon, C.A. (1994) A Mössbauer milliprobe: Practical considerations. *Hyperfine Interactions*, 92,
526 1235–1239.
- 527 Meier, T., Trybel, F., Khandarkhaeva, S., Laniel, D., Ishii, T., Aslandukova, A., Dubrovinskaia, N., and
528 Dubrovinsky, L. (2022) Structural independence of hydrogen-bond symmetrisation dynamics at
529 extreme pressure conditions. *Nature Communications*, 13, 1–8.
- 530 Nishi, M., Irifune, T., Tsuchiya, J., Tange, Y., Nishihara, Y., Fujino, K., and Higo, Y. (2014) Stability of
531 hydrous silicate at high pressures and water transport to the deep lower mantle. *Nature Geoscience*,
532 7, 224–227.
- 533 Nishi, M., Tsuchiya, J., Arimoto, T., Kakizawa, S., Kunimoto, T., Tange, Y., Higo, Y., and Irifune, T.
534 (2018) Thermal equation of state of MgSiO_4H_2 phase H determined by in situ X-ray diffraction
535 and a multianvil apparatus. *Physics and Chemistry of Minerals*, 45, 995–1001.
- 536 Ohira, I., Ohtani, E., Sakai, T., Miyahara, M., Hirao, N., Ohishi, Y., and Nishijima, M. (2014) Stability
537 of a hydrous δ -phase, $\text{AlOOH-MgSiO}_2(\text{OH})_2$, and a mechanism for water transport into the base of
538 lower mantle. *Earth and Planetary Science Letters*, 401, 12–17.
- 539 Ohira, I., Jackson, J.M., Solomatova, N. V., Sturhahn, W., Finkelstein, G.J., Kamada, S., Kawazoe, T.,
540 Maeda, F., Hirao, N., Nakano, S., and others (2019) Compressional behavior and spin state of δ -

- 541 (Al,Fe)OOH at high pressures. *American Mineralogist*, 104, 1273–1284.
- 542 Ohtani, E., Amaike, Y., Kamada, S., Sakamaki, T., and Hirao, N. (2014) Stability of hydrous phase H
543 MgSiO₄H₂ under lower mantle conditions. *Geophysical Research Letters*, 41, 8283–8287.
- 544 Pamato, M.G., Myhill, R., Boffa Ballaran, T., Frost, D.J., Heidelbach, F., and Miyajima, N. (2015)
545 Lower-mantle water reservoir implied by the extreme stability of a hydrous aluminosilicate. *Nature*
546 *Geoscience*, 8, 75–79.
- 547 Prescher, C., McCammon, C., and Dubrovinsky, L. (2012) *MossA* : a program for analyzing energy-
548 domain Mössbauer spectra from conventional and synchrotron sources. *Journal of Applied*
549 *Crystallography*, 45, 329–331.
- 550 Ralph, R.L., and Finger, L.W. (1982) A Computer-Program for Refinement of Crystal Orientation
551 Matrix and Lattice-Constants from Diffractometer Data with Lattice Symmetry Constraints. *Journal*
552 *of Applied Crystallography*, 15, 537–539.
- 553 Rosa, A.D., Sanchez-Valle, C., and Ghosh, S. (2012) Elasticity of phase D and implication for the
554 degree of hydration of deep subducted slabs. *Geophysical Research Letters*, 39, 6–11.
- 555 Rosa, A.D., Mezouar, M., Garbarino, G., Bouvier, P., Ghosh, S., Rohrbach, A., and Sanchez-Valle, C.
556 (2013) Single-crystal equation of state of phase D to lower mantle pressures and the effect of
557 hydration on the buoyancy of deep subducted slabs. *Journal of Geophysical Research: Solid Earth*,
558 118, 6124–6133.
- 559 Sano-Furukawa, A., Kagi, H., Nagai, T., Nakano, S., Fukura, S., Ushijima, D., Iizuka, R., Ohtahtani,
560 E., and Yagi, T. (2009) Change in compressibility of δ -AlOOH and δ -AlOOD at high pressure: A
561 study of isotope effect and hydrogen-bond symmetrization. *American Mineralogist*, 94, 1255–1261.

- 562 Sano-Furukawa, A., Hattori, T., Komatsu, K., Kagi, H., Nagai, T., Molaison, J.J., dos Santos, A.M., and
563 Tulk, C.A. (2018) Direct observation of symmetrization of hydrogen bond in δ -AlOOH under
564 mantle conditions using neutron diffraction. *Scientific Reports*, 8, 1–9.
- 565 Satta, N., Criniti, G., Kurnosov, A., Boffa Ballaran, T., Ishii, T., and Marquardt, H. (2021) High-
566 Pressure Elasticity of δ -(Al,Fe)OOH Single Crystals and Seismic Detectability of Hydrous MORB
567 in the Shallow Lower Mantle. *Geophysical Research Letters*, 48, 1–10.
- 568 Sheldrick, G.M. (2015a) Crystal structure refinement with SHELXL. *Acta Crystallographica Section C:*
569 *Structural Chemistry*, 71, 3–8.
- 570 ——— (2015b) Foundations and Advances SHELXT-Integrated space-group and crystal-structure
571 determination. *Acta Cryst*, 71, 3–8.
- 572 Shen, G., Wang, Y., Dewaele, A., Wu, C., Fratanduono, D.E., Eggert, J., Klotz, S., Dziubek, K.F.,
573 Loubeyre, P., Fat'yanov, O. V., and others (2020) Toward an international practical pressure scale:
574 A proposal for an IPPS ruby gauge (IPPS-Ruby2020). *High Pressure Research*, 1–16.
- 575 Tanabe, Y., and Sugano, S. (1954) On the Absorption Spectra of Complex Ions. I. *Journal of the*
576 *Physical Society of Japan*, 9, 753–766.
- 577 Vinet, P., Rose, J.H., Ferrante, J., and Smith, J.R. (1989) Universal features of the equation of state of
578 solids. *Journal of Physics: Condensed Matter*, 1, 1941–1963.
- 579 Wu, X., Wu, Y., Lin, J.-F., Liu, J., Mao, Z., Guo, X., Takashi, Y., McCammon, C., Prakapenka, V.B.,
580 and Xiao, Y. (2016) Two-stage spin transition of iron in FeAl-bearing phase D at lower mantle.
581 *Journal of Geophysical Research: Solid Earth*, 121, 6411–6420.
- 582 Xu, C., Gréaux, S., Inoue, T., Noda, M., Sun, W., Kuwahara, H., and Higo, Y. (2020) Sound Velocities

583 of Al-Bearing Phase D up to 22 GPa and 1300 K. Geophysical Research Letters, 47, 1–10.
584 Yang, H., Prewitt, C.T., and Frost, D.J. (1997) Crystal structure of the dense hydrous magnesium
585 silicate, phase D. American Mineralogist, 82, 651–654.

586

587

588

Figure captions

589 **Figure 1.** Mössbauer spectrum of Fe-bearing Al-phase D. The spectrum was fit to a single Lorentzian
 590 doublet that was assigned to octahedrally coordinated Fe^{3+} (blue area). The asymmetry of the doublet
 591 likely arises from the fact that the sample consisted of a mosaic of few single crystals, rather than a fine
 592 powder with completely randomly orientated crystallites. Although the candidate $P6_322$ and $P\bar{3}1m$ space
 593 groups have multiple octahedral sites occupied by Fe^{3+} , we used a single Lorentzian doublet to fit the
 594 transmission spectrum due to the non-distorted shape of octahedra and very similar volumes of the latter
 595 (similar crystal field).

596 **Figure 2.** Unwarp images of the reciprocal space of Fe-bearing Al-phase D samples obtained from single-
 597 crystal X-ray diffraction measurements *in-house* (a,b) and at the ECB P02.2 in Hamburg (c,d). When $l =$
 598 $2n$ (e.g. $hk0$ in a and c), no diffuse scattering is observed between neighboring reflections. When $l = 2n +$
 599 1 (e.g. $hk1$ in b and d) diffuse scattering streaks are observed between neighboring reflection for which h
 600 $- k \neq 3n$. The black dot at the center of each image denotes the origin of the plane in reciprocal space.
 601 Black circles in (d) denote reflections from the diamond anvil where the crystal was placed in order to be
 602 measured at the ECB P02.2.

603 **Figure 3.** Volume (a) and axial (b) compression data of Fe-bearing Al-phase D collected over two separate
 604 runs. Solid squares and diamonds represent the high spin phase, while open diamonds represent the low
 605 spin phase. Error bars are not shown as they are smaller than the symbols. Solid lines represent 3rd-order
 606 Birch-Murnaghan (BM3) equations of state (EOS) fits between 0 and 38 GPa, while the dashed line in (a)
 607 indicates the modified BM3 EOS fit of all data accounting for the spin-crossover of Fe^{3+} . In the inset in
 608 (a), the population of the three most relevant electronic states is modelled as a function of pressure based
 609 on the crystal field parameters used to fit the P - V data. The inset in (b) shows that the c/a ratio of Fe-

610 bearing Al-phase D only slightly decreases with pressure and is barely affected by the onset of the spin
611 crossover.

612

Tables

Table 1. Unit-cell lattice parameters of Fe-bearing Al-phase D as a function of pressure. P was calculated as the mean between values measured before and after XRD measurements using the ruby fluorescence shift (Shen et al., 2020), with σP being their semi-difference.

| Run number | P (GPa) | σP (GPa) | a (Å) | σa (Å) | c (Å) | σc (Å) | V (Å ³) | σV (Å ³) |
|---------------|--------------|---------------------|------------|-------------------|------------|-------------------|--------------------------|---------------------------------|
| 1 | 0.35 | 0.02 | 4.7430 | 0.0005 | 4.2873 | 0.0003 | 83.525 | 0.017 |
| 1 | 1.02 | 0.02 | 4.7376 | 0.0004 | 4.2797 | 0.0005 | 83.186 | 0.015 |
| 1 | 3.35 | 0.08 | 4.7172 | 0.0004 | 4.2577 | 0.0004 | 82.050 | 0.015 |
| 1 | 5.25 | 0.07 | 4.7020 | 0.0006 | 4.2408 | 0.0005 | 81.196 | 0.016 |
| 1 | 7.56 | 0.08 | 4.6850 | 0.0004 | 4.2215 | 0.0003 | 80.247 | 0.016 |
| 1 | 10.66 | 0.08 | 4.6653 | 0.0004 | 4.2000 | 0.0003 | 79.165 | 0.016 |
| 1 | 13.64 | 0.16 | 4.6435 | 0.0004 | 4.1774 | 0.0003 | 78.007 | 0.012 |
| 1 | 16.44 | 0.04 | 4.6263 | 0.0006 | 4.1604 | 0.0004 | 77.112 | 0.016 |
| 1 | 18.36 | 0.09 | 4.6148 | 0.0004 | 4.1482 | 0.0003 | 76.506 | 0.011 |
| 1 | 19.16 | 0.08 | 4.6088 | 0.0004 | 4.1427 | 0.0003 | 76.205 | 0.012 |
| 1 | 21.41 | 0.08 | 4.5958 | 0.0004 | 4.1294 | 0.0003 | 75.535 | 0.011 |
| 1 | 24.66 | 0.23 | 4.5779 | 0.0005 | 4.1120 | 0.0003 | 74.631 | 0.013 |
| 1 | 27.66 | 0.11 | 4.5617 | 0.0005 | 4.0964 | 0.0004 | 73.821 | 0.014 |
| 1 | 30.50 | 0.12 | 4.5481 | 0.0007 | 4.0835 | 0.0004 | 73.152 | 0.017 |
| 1 | 32.79 | 0.09 | 4.5346 | 0.0006 | 4.0717 | 0.0004 | 72.509 | 0.015 |
| 1 | 35.32 | 0.10 | 4.5234 | 0.0007 | 4.0595 | 0.0005 | 71.935 | 0.017 |
| 1 | 37.92 | 0.09 | 4.5101 | 0.0007 | 4.0475 | 0.0005 | 71.302 | 0.018 |
| 2 | 5.84 | 0.02 | 4.6985 | 0.0002 | 4.2356 | 0.0013 | 80.98 | 0.02 |
| 2 | 9.23 | 0.02 | 4.6715 | 0.0002 | 4.2093 | 0.0013 | 79.55 | 0.02 |
| 2 | 23.07 | 0.04 | 4.5852 | 0.0003 | 4.1200 | 0.0020 | 75.01 | 0.04 |
| 2 | 33.30 | 0.05 | 4.5295 | 0.0005 | 4.0715 | 0.0018 | 72.36 | 0.03 |
| 2 | 40.75 | 0.05 | 4.4912 | 0.0006 | 4.0300 | 0.0020 | 70.43 | 0.04 |
| 2 | 42.42 | 0.05 | 4.4840 | 0.0007 | 4.0215 | 0.0020 | 70.05 | 0.04 |
| 2 | 45.96 | 0.05 | 4.4677 | 0.0006 | 4.0060 | 0.0020 | 69.27 | 0.03 |
| 2 | 49.41 | 0.08 | 4.4509 | 0.0006 | 3.9890 | 0.0020 | 68.47 | 0.04 |
| 2 | 52.41 | 0.05 | 4.4372 | 0.0006 | 3.9780 | 0.0030 | 67.91 | 0.05 |

Table 2. Fit parameters of 3rd-order Birch-Murnaghan, Vinet, and spin-crossover equations of state for Fe-bearing Al-phase D. Values in italics were fixed in the fit.

| Low-spin state EOS | | | | | | | | | | |
|--------------------|-----------------------|-------------------------|----------------|-----------|--------------|-------------------|-----------|-----------|-------------------|-----------|
| EOS type | P range (GPa) | V_0 (Å ³) | K_{T0} (GPa) | K'_{T0} | a_0 (Å) | M_{a0} (GPa) | M'_{a0} | c_0 (Å) | M_{c0} (GPa) | M'_{c0} |
| BM3 | 0-38 | 83.68(2) | 166.3(15) | 4.46(12) | 4.7460(9) | 539(10) | 12.6(7) | 4.2904(3) | 421(4) | 15.1(3) |
| Vinet | 0-38 | 83.68(2) | 165.5(15) | 4.62(12) | 4.7460(8) | 537(10) | 13.0(7) | 4.2905(3) | 418(3) | 15.7(3) |
| Spin-crossover EOS | | | | | | | | | | |
| EOS type | P range (GPa) | V_0 (Å ³) | K_{T0} (GPa) | K'_{T0} | Δ_0 | B_0 | δ | $b=c$ | C/B | |
| BM3+SC | 0-53 | 83.71(2) | 161(2) | 5.2(2) | <i>14750</i> | 627(6) | 2.5(2) | -2 | <i>4.73</i> | |

623

624 **Table 3.** Fit parameters of Birch-Murnaghan equations of states of phase D solid solutions from the present and previous studies.

625 Numbers in italics were fixed in the fitting procedure. XRPD: powder X-ray diffraction. BS: Brillouin spectroscopy. SCXRD: single-

626 crystal X-ray diffraction. UI: ultrasonic interferometry. DAC: diamond anvil cell. LVP: large volume press.

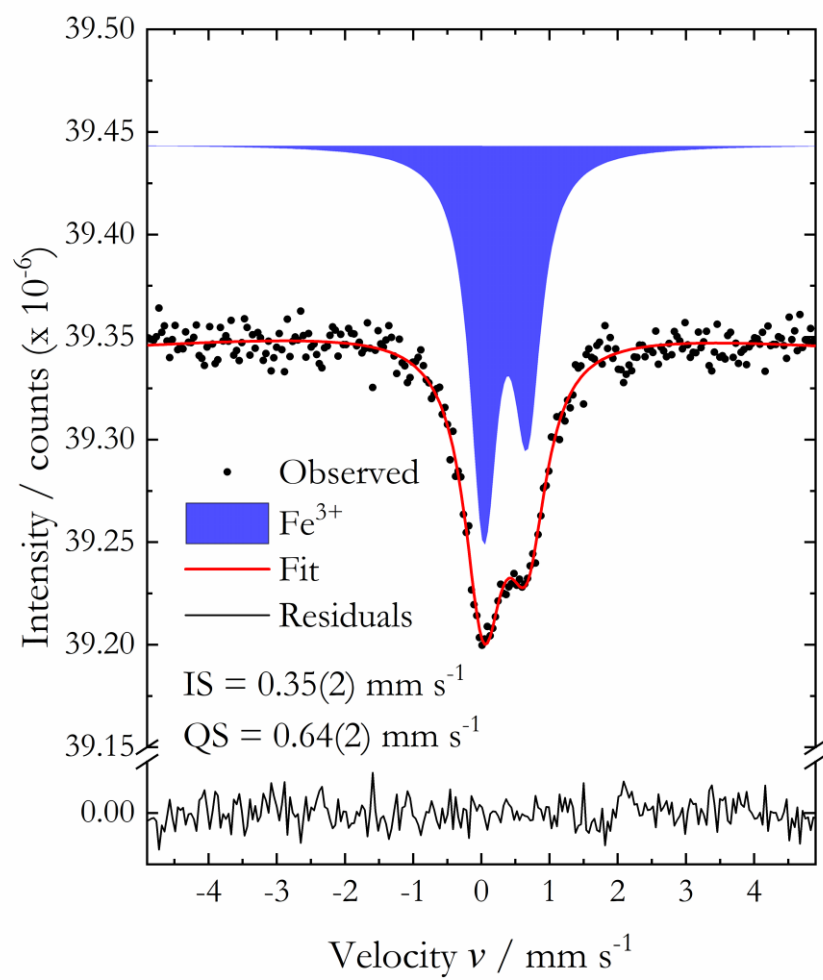
| Composition | V_0 (Å ³) | K_{T0} (GPa) | K'_{T0} | P range (GPa) | Method | Reference |
|--|-------------------------|----------------|-----------|-----------------|--------------|-----------------------|
| Mg _{1.11} Si _{1.6} O ₆ H _{3.6} | 85.66(1) | 166(3) | 4.1(3) | 0-30 | XRPD in DAC | Frost & Fei (1999) |
| Mg _{1.0} Si _{1.7} O ₆ H _{3.0} | 85.1(2) | 168(9) | 4.3(5) | 0-56 | XRPD in DAC | Hushur et al. (2011) |
| Mg _{1.0} Si _{1.7} O ₆ H _{3.0} | 85.4(3) | 150(9) | 5.5(4) | 0-30 | XRPD in DAC | Hushur et al. (2011) |
| Mg _{1.1} Si _{1.9} O ₆ H _{2.4} | 85.6(2) | 149(3) | - | 0 | BS | Rosa et al. (2012) |
| Mg _{1.00} Fe _{0.11} Al _{0.03} Si _{1.90} O ₆ H _{2.50} | 85.1(2) | 153(4) | - | 0 | BS | Rosa et al. (2012) |
| Mg _{0.89} Fe _{0.14} Al _{0.25} Si _{1.56} O ₆ H _{2.93} | 86.10(5) | 137(3) | 6.3(3) | 0-30 | XRPD in LVP | Litasov et al. (2007) |
| Mg _{0.99} Fe _{0.12} Al _{0.09} Si _{1.75} O ₆ H _{2.51} | 85.32 (2) | 142(3) | 6.2(4) | 0-20 | XRPD in LVP | Litasov et al. (2008) |
| Mg _{1.1} Si _{1.8} O ₆ H _{2.5} | 85.80(5) | 151.4(1.2) | 4.89(8) | 0-65 | SCXRD in DAC | Rosa et al. (2013) |
| Mg _{1.00} Fe _{0.15} Al _{0.09} Si _{1.75} O ₆ H _{2.51} | 86.14(3) | 147(2) | 6.3(3) | 0-40 | SCXRD in DAC | Chang et al. (2013) |
| Mg _{1.14} Si _{1.73} O ₆ H _{2.81} | 85.07(4) | 179(1) | 4 | 0-80 | SCXRD in DAC | Wu et al. (2016) |
| Mg _{0.89} Fe _{0.11} Al _{0.37} Si _{1.55} O ₆ H _{2.65} | 85.7(1) | 169(2) | 4 | 0-37 | SCXRD in DAC | Wu et al. (2016) |
| Mg _{0.83} Al _{0.60} Si _{1.20} O ₆ H _{2.89} | 86.71 | 143(4) | 5.8(7) | 0-25 | XRPD in LVP | Xu et al. (2020) |
| Mg _{0.83} Al _{0.60} Si _{1.20} O ₆ H _{2.89} | 86.71 | 144(5) | 5.5(7) | 0-25 | UI in LVP | Xu et al. (2020) |
| Fe _{0.22} Al _{1.53} Si _{0.86} O ₆ H _{3.33} | 83.68(2) | 166.3(1.5) | 4.46(12) | 0-38 | SCXRD in DAC | this study |

627

628

629

630 Figure 1

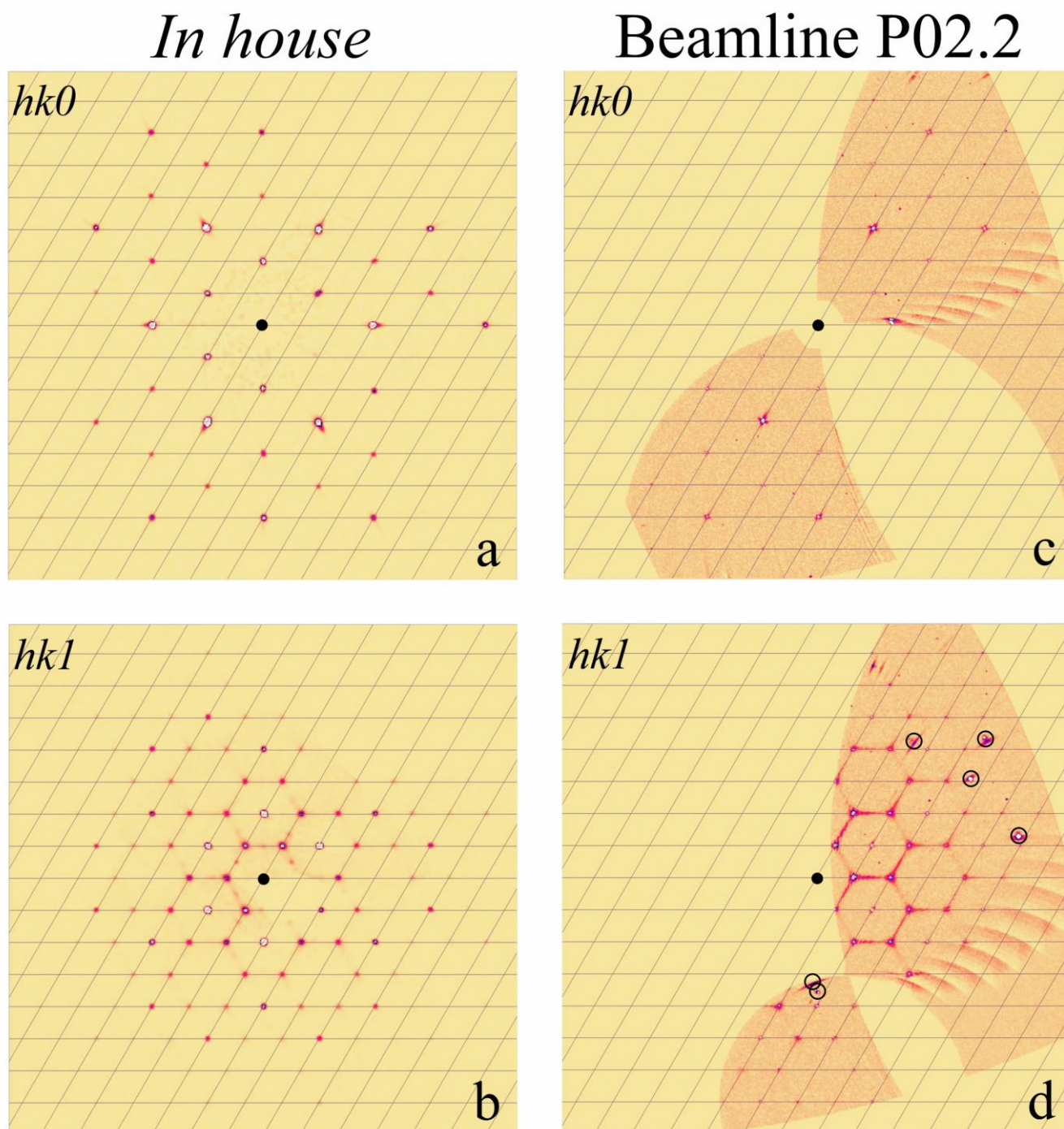


631

632

633

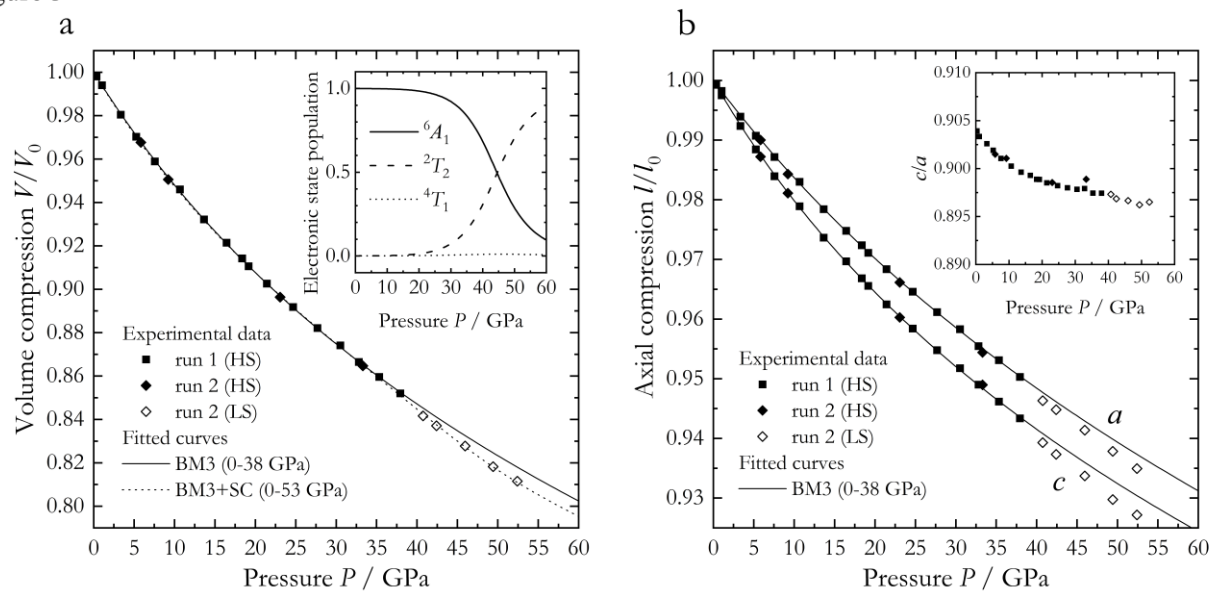
634 Figure 2



635

636

Figure 3



637

638